CFD Modeling of a Bubble Column Reactor Carrying out a Consecutive A → B → C Reaction

By *J. M. van Baten* and *R. Krishna**

In this paper, we develop a CFD model for describing a bubble column reactor for carrying out a consecutive first-order reaction sequence A → B → C. Three reactor configurations, all operating in the homogeneous bubbly regime, were investigated: (I) column diameter D_T = 0.1 m, column height H_T = 1.1 m, (II) D_T = 0.1 m, H_T = 2 m, and (III) D_T = 1 m, H_T = 5 m. Eulerian simulations were carried out for superficial gas velocities U_G in the range of 0.005–0.04 m/s, assuming cylindrical axisymmetry. Additionally, for configurations I and III fully three-dimensional transient simulations were carried out for checking the assumption of cylindrical axisymmetry. For the 0.1 m diameter column (configuration I), 2-D axisymmetric and 3-D transient simulations yield nearly the same results for gas holdup ε_G, centerline liquid velocity $V_L(0)$, conversion of A, χ_A, and selectivity to B, S_B. In sharp contrast, for the 1 m diameter column (configuration III), there are significant differences in the CFD predictions of ε_G, $V_L(0)$, χ_A, and S_B using 2-D and 3-D simulations; the 2-D strategies tend to exaggerate $V_L(0)$, and underpredict ε_G, χ_A, and S_B. The transient 3-D simulation results appear to be more realistic. The CFD simulation results for χ_A and S_B are also compared with a simple analytic model, often employed in practice, in which the gas phase is assumed to be in plug flow and the liquid phase is well mixed. For the smaller diameter columns (configurations I and II) the CFD simulation results for χ_A are in excellent agreement with the analytic model, but for the larger diameter column the analytic model is somewhat optimistic. There are two reasons for this deviation. Firstly, the gas phase is not in perfect plug flow and secondly, the liquid phase is not perfectly mixed. The computational results obtained in this paper demonstrate the power of CFD for predicting the performance of bubble column reactors. Of particular use is the ability of CFD to describe scale effects.

1 Introduction

Bubble columns are widely used in industry for carrying out a variety of chemical reactions such as hydrogenations, oxidations and the Fischer-Tropsch synthesis. Many recent experimental studies have emphasised the strong influence of column diameter on bubble column hydrodynamics [1,2]. In particular, the strength of the liquid circulations increases significantly with increasing column diameter and, as a consequence, the liquid phase tends to approach well-mixed conditions. In the wall regions, the down-flowing liquid tends to drag the gas bubbles downwards whereas the gas bubbles are accelerated in the central core region; both these factors contribute to significant deviations from the plug flow assumption for the gas phase.

One commonly used approach to the calculation of the conversion, and selectivity, in bubble column reactors is to assume that the gas phase traverses the reactor in plug flow and that the liquid phase is well mixed [3]. Refinements to this approach involve the use of the axial dispersion model for either, or both, fluid phases [3,4]. The major disadvantage of this approach is that we need reliable information on the axial dispersion coefficients in the gas and liquid phases as a function of column geometry and operating conditions. While there are several studies on liquid phase axial dispersion coefficients [5–7], information on the scale influence of the gas phase dispersion is much more scarce, and less reliable [8]. Another point to stress is that the dispersion characteristics of the gas and liquid phases are interrelated and it is essential to use a consistent model to estimate these parameters. Very few of the empirical correlations in the literature [3] are based on a physically consistent model for bubble column hydrodynamics.

Several recent publications have established the potential of computational fluid dynamics (CFD) in the Eulerian framework for describing the hydrodynamics of bubble columns [9–14]. These CFD models are developed for either the homogeneous [11–13,15] or heterogeneous [16] flow regimes. By their very nature, CFD models offer a consistent physical basis for the description of bubble column hydrodynamics and provide a good platform for estimation of the conversion taking nonideal flow behavior of the fluid phases, without the necessity of resorting to the axial dispersion model. Our earlier publications had validated the Eulerian simulation strategy for describing the hydrodynamics [15,17,18] and liquid dispersion [19] by comparison with experimental data. None of the published CFD models in the literature has focused on either the reaction or mass transfer performance of bubble column reactors.

The major objective of the present communication is to develop a CFD model to describe a bubble column reactor for carrying out a consecutive first-order reaction sequence A → B → C and to underline the strong influence of scale on the reactor conversion and selectivity. We restrict our model development to the homogeneous bubbly flow regime of operation.

[*] J. M. van Baten, R. Krishna (krishna@science.uva.nl), Department of Chemical Engineering, University of Amsterdam, Nieuwe Achtergracht 166, 1018 WV Amsterdam, The Netherlands.

  DOI: 10.1002/ceat.200401968 *Chem. Eng. Technol.* **2004**, *27*, No. 4

2 Development of CFD Model

Simulations were carried out for three different geometries with respect to column diameter D_T and column height H_T as specified in Tab. 1, along with details of the computational grids for two-dimensional (2-D) cylindrical axisymmetric simulations for cocurrent upflow of gas and liquid phases (see also Fig. 1)[1]. Additionally, for configurations I (D_T = 0.1 m, H_T = 1.1 m) and III (D_T = 1 m, H_T = 5 m) fully

Table 1. Details of computational grids for the three columns. The grid details below are for cylindrical axisymmetric simulations (2-D). For 3-D transient simulations, 10 cells in the azimuthal direction were chosen and so the total number of cells were 10 times higher than those for the corresponding 2-D simulations. The fine grid was used for just one 2-D simulation with configuration III, with U = 0.03 m/s.

Configuration	Column diameter D_T/[m]	Total column height H_T/[m]	Observation height H_{obs}/[m]	Number of cells in radius	Number of cells in height	Total number of cells
I	0.10	1.1	1.0	30	110	3,300
II	0.10	2.0	1.8	30	200	6,000
III	1.00	5.0	4.5	50	250	12,500
III (fine grid)	1.00	5.0	4.5	70	300	21,000

three-dimensional (3-D) transient simulations, with 10 cells in the azimuthal direction, were carried out for checking the assumption of cylindrical axisymmetry. In all the simulations, the superficial liquid velocity U_L at the bottom inlet was maintained at 0.001 m/s. The superficial gas velocity U_G at the bottom inlet was varied in the range 0.005–0.04 m/s. The physical and transport properties of the gas and liquid phases are specified in Tab. 2. In each case three different types of simulations were carried out.

– Determination of the steady-state (or quasi-steady-state in the case of fully 3-D case) *hydrodynamics.*
– Determination of the interphase *mass transfer* by introducing a soluble, nonreactive, component (tracer) in the gas phase.
– Determination of the conversion and selectivity for the liquid phase *reaction* A → B → C, with the reactant A introduced into the reactor via the gas inlet. The components B and C were assumed to be present only in the liquid phase.

We discuss the modeling of the three steps, in turn.

2.1 CFD Modeling of Bubble Column Hydrodynamics

For either fluid phase in the bubble column reactor, the volume-averaged mass and momentum conservation equations in the Eulerian framework are given by

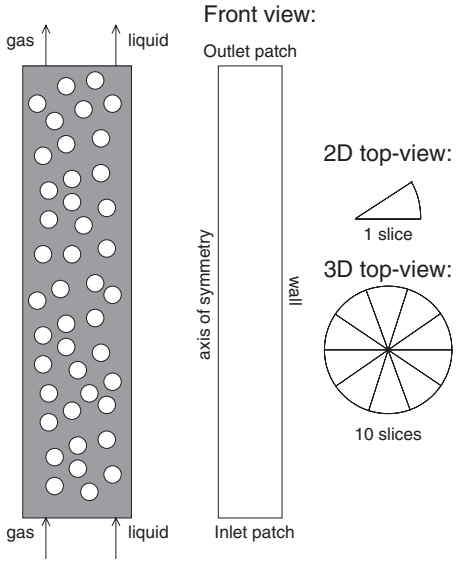

Figure 1. Schematic overview of the computational domains, including front and top views.

Table 2. Properties used in the CFD simulations.

	Liquid (water)	Gas (air)
Viscosity, μ/[Pa s]	1×10^{-3}	1.7×10^{-5}
Diffusivity of tracer, or A or B, $\mathcal{D}$/[m^2 s^{-1}]	1×10^{-9}	1.0×10^{-5}
Density, ρ/[kg/m^3]	998	1.3
Interphase mass transfer coefficient, k_L/[m/s]	0.0004	
Henry coefficient, He/[–]	0.05	
Surface tension, σ/[N/m]	0.073	

$$\frac{\partial\left(\varepsilon_k \rho_k\right)}{\partial t} + \nabla \bullet \left(\rho_k \varepsilon_k \mathbf{u}_k\right) = 0 \tag{1}$$

$$\frac{\partial\left(\rho_k \varepsilon_k \mathbf{u}_k\right)}{\partial t} + \nabla \bullet \left(\rho_k \varepsilon_k \mathbf{u}_k \mathbf{u}_k\right) = \mu_{k,eff}\ \varepsilon_k \left(\nabla \mathbf{u}_k + \left(\nabla \mathbf{u}_k\right)^T\right) - \varepsilon_k \nabla p + \mathbf{M}_{kl} + \rho_k \varepsilon_k \mathbf{g} \tag{2}$$

where, ρ_k, $\mathbf{u}_k$, and ε_k represent, respectively, the macroscopic density, velocity, and volume fraction of phase k; $\mu_{k,eff}$ is the effective viscosity of the fluid phase k, including the molecular and turbulent contributions; p is the pressure, $\mathbf{M}_{kl}$, the interphase momentum exchange between phase k and phase l and $\mathbf{g}$ is the gravitational acceleration.

The momentum exchange between the gas (subscript G) and liquid phase (subscript L) phases is given by

$$\mathbf{M}_{L,G} = \frac{3}{4}\rho_L \frac{\varepsilon_G}{d_b} C_D \left(\mathbf{u}_G - \mathbf{u}_L\right)\left|\mathbf{u}_G - \mathbf{u}_L\right| \tag{3}$$

We have only included the drag force contribution to $\mathbf{M}_{L,G}$, in keeping with the works of Sanyal *et al.* [12] and Sokolichin and Eigenberger [13]. The added mass and lift forces have been ignored in the present analysis.

1) List of symbols at the end of the paper.

The interphase drag coefficient is calculated from [20]:

$$C_D = \frac{2}{3}\sqrt{\text{Eö}} \tag{4}$$

where the Eötvös number is defined as

$$\text{Eö} = \frac{g(\rho_L - \rho_G)d_b^2}{\sigma} \tag{5}$$

where d_b is the equivalent diameter of the bubbles. The bubble diameter is taken to be 0.005 m, a typical value for air-water systems operating in the homogeneous bubbly flow regime.

For the continuous, liquid, phase, the turbulent contribution to the stress tensor is evaluated by means of the k-ε model, using standard single-phase parameters C_μ = 0.09, $C_{1\varepsilon}$ = 1.44, $C_{2\varepsilon}$ = 1.92, σ_k = 1 and σ_ε = 1.3. The applicability of the k-ε model has been considered in detail by Sokolichin and Eigenberger [13]. No turbulence model is used for calculating the velocity fields of the dispersed gas bubbles.

A commercial CFD package CFX, versions 4.2 and 4.4, of ANSYS Inc., Canonsburg, USA, was used to solve the equations of continuity and momentum. This package is a finite volume solver, using body-fitted grids. The grids are non-staggered and all variables are evaluated at the cell centers. An improved version of the Rhie-Chow algorithm [21] is used to calculate the velocity at the cell faces. The pressure-velocity coupling is obtained using the SIMPLEC algorithm [22]. For the convective terms in Eqs. (1) and (2), hybrid differencing was used. A fully implicit backward differencing scheme was used for the time integration.

At the inlet patch, superficial liquid velocity U_L and superficial gas velocity U_G were maintained by setting the liquid holdup to $\varepsilon_L = U_L/(U_G + U_L)$, the gas holdup to $\varepsilon_G = 1 - \varepsilon_L$, and the velocities of both phases to $\mathbf{u}_{G,z} = \mathbf{u}_{L,z} = (U_L + U_G)$. At the outlet at the top, the gas holdup was set to $\varepsilon_{G,top}$, and the liquid holdup to $1 - \varepsilon_{G,top}$. The outlet velocities were specified as $\mathbf{u}_{G,z} = U_G/\varepsilon_{G,top}$ and $\mathbf{u}_{L,z} = U_L/(1 - \varepsilon_{G,top})$. The gas holdup at the outlet patch at the top was chosen 5 %. It was verified that the gas holdup at the top had negligible influence on the results; the holdup and velocities near the top are adjusted to equilibrium values in a very short distance from the top, having little effect on the system average values. Moreover, all values reported are at a distance far enough from the top not to be influenced significantly by the choice of $\varepsilon_{G,top}$, see the specification of the observation heights in Tab. 1. The gas and liquid phase were injected uniformly over the inner 80 % of the bottom patch. At the walls, no-slip boundary conditions were applied.

The time stepping strategy used in all simulations was 100 steps at 5×10^{-5} s, 100 steps at 1×10^{-4} s, 100 steps at 5×10^{-4} s, 100 steps at 1×10^{-3} s, 200 steps at 3×10^{-3} s, 1400 steps at 5×10^{-3} s, and the remaining steps until quasi-steady state is achieved at 1×10^{-2} s. For each run, the hydrodynamics was solved first in a transient manner until steady state was reached. Steady state was indicated by a situation in which all of the variables remained constant; a typical approach to steady state is illustrated for the centerline liquid velocity $V_L(0)$ in Fig. 2(a) for configuration I for 2-D axisymmetric and 3-D simulations. In the case of 3-D simulations, the simulations were run long enough to allow the determination of time-averaged hydrodynamic parameters in quasi-steady state. For the 0.1 m diameter column, we see that both 2-D and 3-D simulations give similar (quasi-) steady-state values of $V_L(0)$. The situation is completely different for configuration III, of diameter 1 m; see Fig. 2(b). Here, the 2-D axisymmetric and 3-D simulations reach different (quasi-) steady-state values of $V_L(0)$; this is due to the sloshing of the liquid from side to side in the 3-D simulations, as can be evidenced in the animations placed on our website: http://ct-cr4.chem.uva.nl/bccocurrent/. We shall return to this point later when we discuss the simulation results.

2.2 CFD Modeling of Interphase Mass Transfer

The steady state (or quasi-steady-state in the case of 3-D run) results of a hydrodynamic run were used to start a dynamic mass transfer simulation in which the inflowing gas stream is "traced" with a component that is soluble in the liquid phase. The concentration of tracer in the inlet gas is maintained at unity (arbitrary units). The inflowing liquid

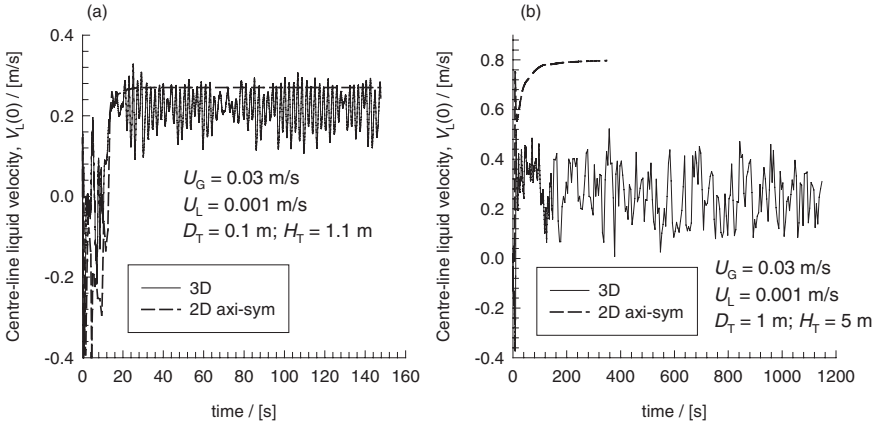

Figure 2. Centerline liquid velocity vs. time for (a) configuration I and (b) configuration III, operating at U_G = 0.03 m/s and U_L = 0.001 m/s. Comparison of 2-D axi-symmetric and transient 3-D simulations. For configuration I, the reported velocities are at 1 m observation height, whereas for configuration III, the observation height is 4.5 m. Typical animations are to be found on our website: http://ct-cr4.chem.uva.nl/bccocurrent/.

stream does not contain any tracer component A.

The following component balance equations are solved for the mass tracer:

$$\frac{\partial}{\partial t}\varepsilon_k \rho_k C_{\alpha,k} + \nabla \cdot \left(\varepsilon_k \rho_k \mathbf{u}_k C_{\alpha,k} - Đ_{\alpha,k}\varepsilon_k \rho \nabla C_{\alpha,k}\right) = \rho_{\alpha,k}(F_{\alpha,kl} + \varepsilon_k r_{\alpha,k}) \quad (6)$$

Here, $C_{\alpha,k}$ is the concentration of mass-tracer component α in phase k, $Đ_{\alpha,k}$ is the diffusion coefficient of mass tracer component α in phase k and $F_{\alpha,kl}$ is the flux of mass tracer component α between phases k and l. The production (or consumption) due to reaction of component α in phase k is denoted by $r_{\alpha,k}$. In the dynamic mass transfer simulations, tracer component α is assumed to be nonreactive, so $r_{\alpha,k} = 0$. The flux $F_{\alpha,GL}$ for liquid phase L and gas phase G are defined as:

$$F_{\alpha,GL} = k_L a(C_{\alpha,G} He - C_{\alpha,L}) \quad (7)$$

Here, k_L is the mass transfer coefficient and He is the Henry coefficient for the mass tracer. The mass transfer coefficient k_L was chosen as 4×10^{-4} m/s. The Henry coefficient He was chosen 0.05. The physical and transport properties of the tracer component are specified in Tab. 2. The relative surface area a is calculated from:

$$a = \frac{6\varepsilon_G}{d_b} \quad (8)$$

No flux of mass tracer is allowed through the walls. To ensure no flux of tracer takes place across flow boundaries with zero ingoing flow, the boundary value for the mass component concentration is set equal to the value inside the computational domain at each iteration for these boundaries.

For the 2-D simulations, the hydrodynamic Eqs. (1) and (2) are no longer solved since the system has reached a true steady state; none of the hydrodynamic variables are subject to change any longer. For the 3-D simulations, however, the hydrodynamic equations still need to be calculated. Time steps of 0.1 s were taken, until the tracer concentrations in the system attained (quasi-) steady state. Typical transience of the gas and liquid phase concentrations is shown in Fig. 3, for both 2-D and 3-D simulations of configuration III, operating at $U_G = 0.03$ m/s.

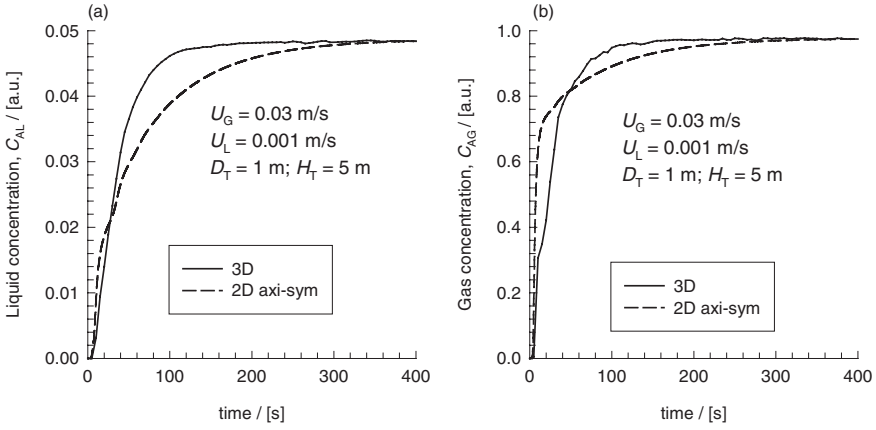

Figure 3. Typical tracer response (mass transfer campaign) for the liquid and the gas phases for configuration III in both 2-D and 3-D simulation strategies (H_T = 5 m, D_T = 1 m, U_G = 0.03 m/s, U_L = 0.001 m/s). In (a) the liquid, and (b) the gas phase tracer concentrations at observation height of 4.5 m are indicated.

2.3 CFD Modeling of A → B → C Reaction

Two components, **A** and **B** were accounted for in the component balance equations (6); the physical and transport properties of both components were taken to be identical, as specified in Tab. 2. At the start of the reaction run, the gas inlet concentration of **A**, $C_{\mathbf{A},G}$, makes a step from zero to unity (a.u.). The gas inlet concentration $C_{\mathbf{B},G}$ and the liquid inlet concentrations $C_{\mathbf{A},L}$ and $C_{\mathbf{B},L}$ remain zero at all times. Component **A** transfers from the gas to the liquid phase: $k_L = 4 \times 10^{-4}$ m/s, $He = 0.05$. In the liquid phase, component **A** reacts to component **B**, which reacts away to component **C** (component **C** is not simulated, but its concentration can be determined by mass conservation equation). Component **B** is not subject to gas-liquid mass transfer ($k_{L,\mathbf{B}} = 0$), and either reacts away to component **C**, or leaves the system through the liquid phase at the outlet.

The reaction terms in Eq. (6) are:

$$r_{\mathbf{A},L} = -k_{\mathbf{A}} C_{\mathbf{A},L}; \quad r_{\mathbf{B},L} = k_{\mathbf{A}} C_{\mathbf{A},L} - k_{\mathbf{B}} C_{\mathbf{B},L}; \quad r_{\mathbf{A},G} = 0; \quad r_{\mathbf{B},G} = 0 \quad (9)$$

with $k_{\mathbf{A}} = 0.1$ s^{-1} and $k_{\mathbf{B}} = 0.03$ s^{-1}. The choice of the reaction rate constants ensures that for all configurations and operating conditions, interphase mass transfer is the predominant limitation.

In the 2-D simulations of the consecutive reaction, the steady-state velocities and holdups are used as inputs and the conservation equations (1) and (2) are *not* solved. For the 3-D simulations, Eqs. (1), (2) *and* (6) need to be solved simultaneously till the system attains quasi-steady state.

Further details of the numerical techniques used in our CFD simulations have been given in our website: http://ct-cr4.chem.uva.nl/bccocurrent/.

3 Simulation Results

3.1 Results on Hydrodynamics

Let us first compare 2-D axisymmetric and 3-D hydrodynamics of configuration I, operating at U_G = 0.03 m/s; the radial distributions of liquid velocity, gas velocity and gas holdup are shown in Fig. 4. There appears to be only a small difference in the liquid and gas velocity profiles. The radial distribution of gas holdup in the 2-D simulation shows an off-center maximum whereas the 3-D simulation yields a more realistic parabolic holdup distribution. By comparing with experimental data, we had earlier concluded that it is essential to employ 3-D simulations in order to correctly represent the gas holdup distribution [16].

A similar comparison of 2-D axisymmetric and 3-D simulations for configuration III, operating at U_G = 0.03 m/s is seen in Fig. 5. For this large 1 m diameter column, there is a significant difference between 2-D and 3-D simulations of the radial distributions of liquid velocity, gas velocity and gas holdup. Due to significant sloshing of the liquid from side to side, as can be viewed from the animations on our website http://ct-cr4.chem.uva.nl/bccocurrent/, the profiles are much flatter for the 3-D simulations. Fig. 5 also includes the 2-D simulation results obtained with a finer grid (with 21000 grid cells; see Tab. 1). It is clear that the simulations do not depend on the grid size; this was also verified for the reaction simulations to be discussed below. The 2-D simulation predicts a centerline liquid velocity $V_L(0)$ of 0.8 m/s, whereas for the 3-D simulation $V_L(0)$ has a much lower value of 0.24 m/s. Experimental data of Forret *et al.* [2] for air-water system in a 1m diameter column appear to suggest that the 3-D simulations are closer to reality as regards the values of $V_L(0)$. The 3-D simulations predict a much flatter distribution of gas holdup; this is more in line with experimental measurements [2]. Due to the much higher liquid velocities in the 2-D simulations the average gas holdup is much lower than that predicted by the 3-D simulations; ε_G = 0.054 for 2-D vs. ε_G = 0.109 for 3-D.

In Fig. 6(a) the centerline liquid velocity $V_L(0)$ and (b) the gas holdup ε_G data as a function of the superficial gas velocity are compared for all three configurations. The 2-D simulations in the 1 m diameter column predict an unrealistically high $V_L(0)$ and, as a consequence, a significantly lower ε_G than the other simulations. As mentioned in the foregoing, for large diameter columns 2-D axisymmetric simulations are unrealistic. All other simulation results for configurations I, II and III appear to yield results that are close to one another. There appears to be no significant scale effects on gas holdup or on the liquid velocity.

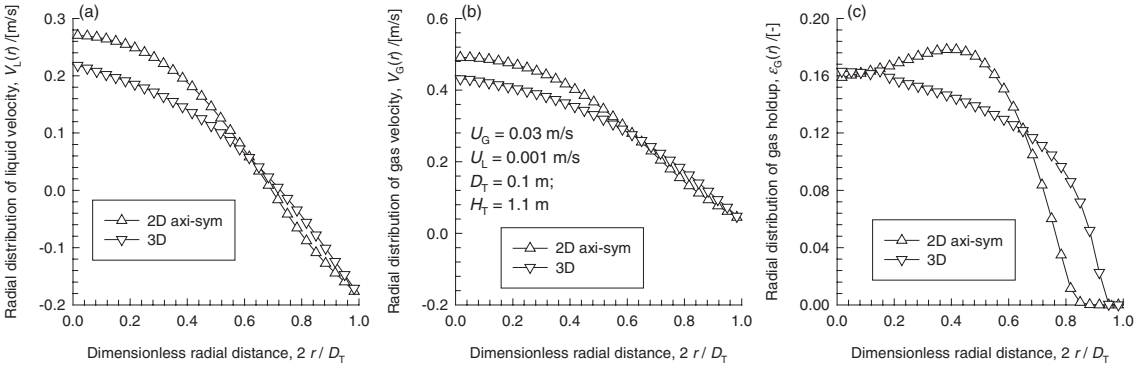

Figure 4. Comparison of 2-D and 3-D simulations for the radial distribution of (a) liquid velocity, (b) gas velocity and (c) gas holdup for configuration I: H_T = 1.1 m, D_T = 0.1 m, U_G = 0.03 m/s, U_L = 0.001 m/s. Reported values are at the observation heights specified in Tab. 1.

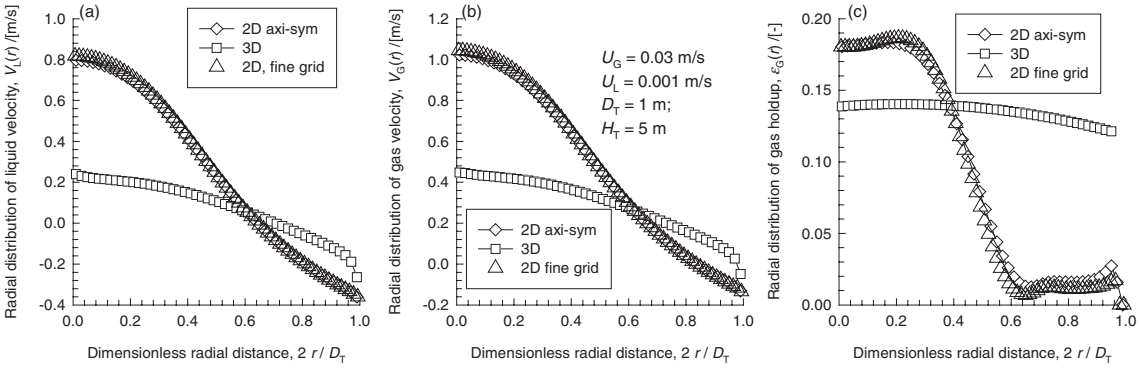

Figure 5. Comparison of 2-D and 3-D simulations for radial distribution of (a) liquid velocity, (b) gas velocity and (c) gas holdup for configuration III: H_T = 5 m, D_T = 1 m, U_G = 0.03 m/s, U_L = 0.001 m/s. Reported values are at the observation heights specified in Tab. 1. Two 2-D simulations are presented, representing 12,500 and 21,000 (fine) grid cells respectively.

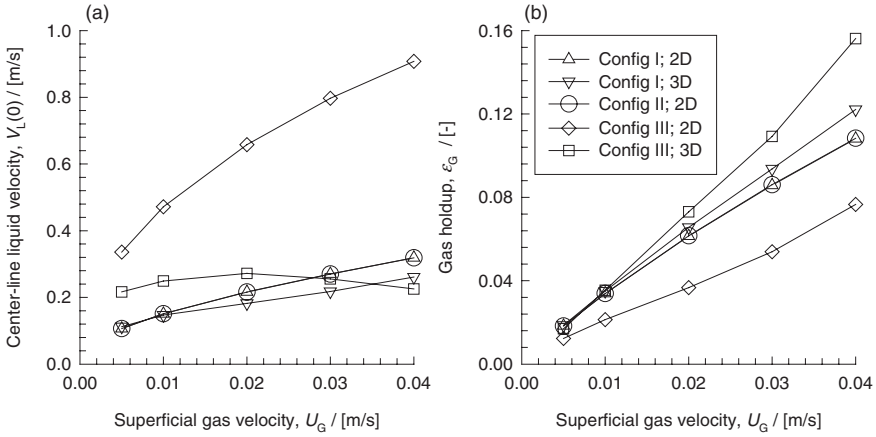

Figure 6. Centerline axial liquid velocity $V_L(0)$ and gas holdup for configurations I, II and III. In all cases $U_L = 0.001$ m/s. Reported values are at the observation heights specified in Tab. 1.

3.2 Results on Interphase Mass Transfer

Fig. 7 shows typical concentration profiles for gas and liquid phases under quasi-steady state from 3-D transient simulation conditions for configuration III operating at $U_G = 0.03$ m/s. We note that the liquid phase cannot be considered to be perfectly well mixed. We also note that depletion in the gas phase concentration is minimal.

In published experimental studies on bubble columns [23,24], the volumetric mass transfer coefficient is usually determined by fitting the transient uptake of a soluble component (e.g., oxygen) in the liquid phase, assuming that the gas phase has a constant concentration, and that the liquid phase is well mixed. This model leads to the following transient response:

$$\frac{C_L}{C_L^*} = 1 - \exp\left(-\frac{k_L a}{1-\varepsilon_G}\, t\right) \qquad (10)$$

where C_L^* is the final, steady-state, value of the liquid concentration. Fig. 7(b) shows a typical transient liquid-phase concentration profile for the 3-D simulation of configuration III, operating at $U_G = 0.03$ m/s. In order to conform with the assumptions underlying Eq. (10), we determined the global average liquid concentration (averaged over both the cross section and the column height) at every time instant. The transient global liquid concentrations are then fitted using Eq. (10) to determine the global value of $k_L a$. For the particular run under consideration, we find $k_L a = 0.026$ s^{-1}, taking the gas holdup $\varepsilon_G = 0.109$ from Fig. 6. This fitted value of $k_L a$ is lower than the "ideal" value of

$$k_L a = 4 \times 10^{-4} \times \frac{6}{0.005} \times 0.109 = 0.052\ \text{s}^{-1}$$

The lower value of the fitted $k_L a$ is primarily attributable to the departure from plug flow behavior of the gas phase. The downflowing liquid drags the bubbles downwards near the wall region.

The fitted values of $k_L a$ for the various configurations are shown in Fig. 8, along with the corresponding values of $(k_L a/\varepsilon_G)$. From the data inputs in the simulations we should expect an "ideal" value

$$\frac{k_L a}{\varepsilon_G} = 4 \times 10^{-4} \times \frac{6}{0.005} = 0.48$$

For low values of U_G, and for $D_T = 0.1$ m we find that the fitted values of $(k_L a/\varepsilon_G)$ exceed 0.48; this is because of the fact that the liquid phase is not entirely backmixed as is assumed in the "ideal" calculation of 0.48. For configuration III with $D_T = 1$ m, the $k_L a/\varepsilon_G$ value is significantly lower than 0.48, due to departure of the gas phase from plug flow caused by strong backmixing of the liquid.

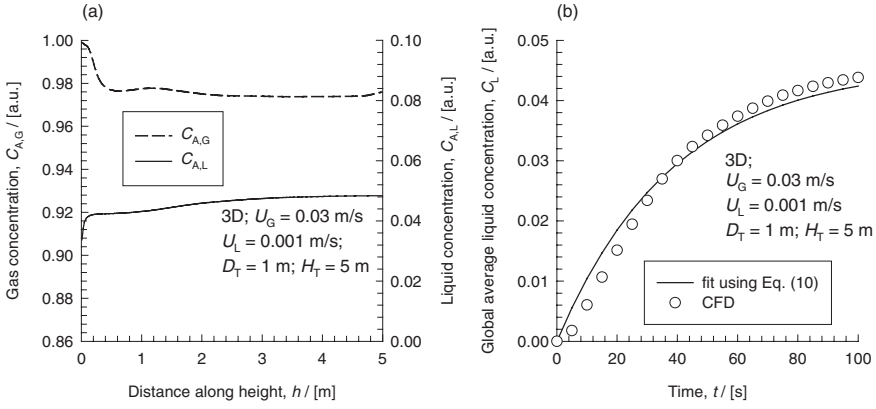

Figure 7. Mass transfer results for 3-D simulation of configuration III ($H_T = 5$ m, $D_T = 1$ m, $U_G = 0.03$ m/s, $U_L = 0.001$ m/s). The concentration at any position is time-averaged over the quasi-steady-state period. (a) Quasi-steady-state concentration profiles for gas and liquid phases. (b) Transient approach to steady state of the global average liquid concentration. The fit to determine $k_L a$, using Eq. (10) is shown as the continuous line.

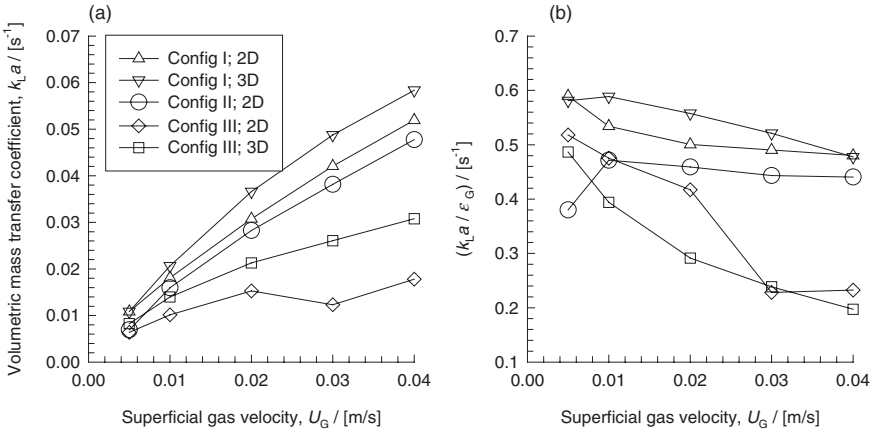

Figure 8. Volumetric mass transfer coefficients $k_L a$ obtained from fitting Eq. (10) for various configurations as a function of the superficial gas velocity. (b) Values of $(k_L a/\varepsilon_G)$ as a function of the superficial gas velocity.

3.3 Results on Conversion and Selectivity of Consecutive Reaction

The CFD simulations yield details of the concentration of A and B in all the grid cells as a function of time. Typical concentration profiles obtained, after cross-sectional area averaging, for A and B along the column height under quasi-steady-state conditions for configuration III are shown in Fig. 9 for operation at U_G = 0.03 m/s. The overall conversion of A, χ_A, can be calculated from the simulations by determining the consumption of A in each grid cell and summing over all cells; these results are shown in Fig. 10(a). The selectivity towards B, i.e. the amount of B produced per amount of A converted, is plotted in Fig. 10(b). For configuration III, it is important to underline the significantly lower conversion anticipated by the 2-D axisymmetric simulation when compared with the transient 3-D simulations. As has been emphasized in the foregoing discussions, the hydrodynamics of large diameter column predicted by the 2-D simulations are unrealistic and the gas holdup values are significantly underpredicted. This lower prediction of gas holdup is reflected in a lower conversion of A.

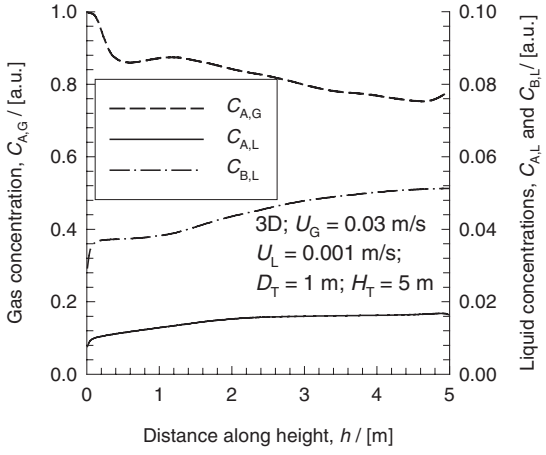

Figure 9. Typical height vs. concentration profiles under quasi-steady state for consecutive reaction simulation campaign using 3-D simulation of configuration III (H_T = 5 m, D_T = 1 m, U_G = 0.03 m/s, U_L = 0.001 m/s).

To gain further insights into the results presented in Fig. 10, we shall consider the "ideal" situation (plug flow of gas and well-mixed liquid phase). For the ideal case, the conversion of A, χ_A, can be calculated analytically from the expression

$$\chi_A = \frac{NRU}{\frac{1}{He} + \frac{(NRU + U_L/U_G)}{1-\exp(-NTU\ He)}} \tag{11}$$

where the dimensionless numbers of mass transfer units NTU and reaction units NRU are defined by

$$NTU = \frac{k_L a\ H_T}{U_G}; \quad NRU = \frac{k_A\ \varepsilon_L\ H_T}{U_G} \tag{12}$$

The selectivity to B can be calculated from

$$S_B = \frac{1}{1 + NRU \frac{U_G k_B}{U_L k_A}} \tag{13}$$

The concentration of A in the liquid stream leaving the reactor is

$$\frac{C_{AL,out}}{C_{AG,in}} = \frac{\chi_A}{NRU} \tag{14}$$

The concentration profile in the gas phase at any height h in the reactor is given by the expression

$$C_{AG}(h) = \left(C_{AG,in} - \frac{C_{AL,out}}{He}\right)\exp\left(-NTU\ He \frac{h}{H_T}\right) + \frac{C_{AL,out}}{He} \tag{15}$$

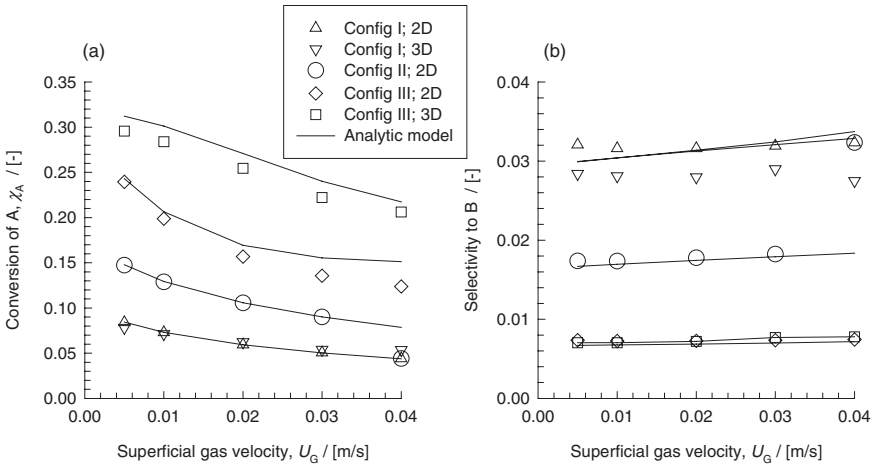

Figure 10. (a) Conversion of A and (b) selectivity towards B, for various configurations. The symbols represent the CFD simulation results. The continuous lines represent the calculation of the analytic model outlined by Eqs (11)–(15). In the analytic calculations the value of the gas holdup ε_G is taken from the individual CFD simulations.

In Fig. 10, the calculations of the conversion of A, and selectivity to B, following Eqs. (11) and (13), are compared with those obtained from CFD simulations. For configurations I and II the agreement between the CFD simulations of χ_A and the analytic model are excellent. For the larger diameter column the agreement is less good, this is because of the departure of the mixing behavior of the gas and liquid phases from the idealized plug flow of gas and well-mixed liquid assumption in the analytic model. In order to underline this, Fig. 11 compares the CFD simulations for the concentrations of A in the liquid and gas phases with the ideal calculations according to Eqs. (14) and (15). We note that the assumptions of well-mixed liquid phase and plug flow of gas phase are both seen not to correspond to the reality mirrored by CFD simulations.

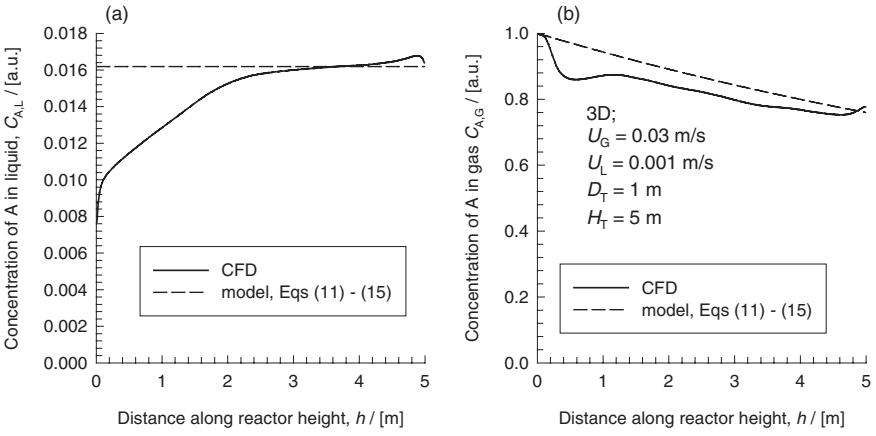

Figure 11. a) Liquid and (b) gas concentrations of reactant A vs. height at steady state for 3-D simulation of configuration III (H_T = 5 m, D_T = 1 m, U_G = 0.03 m/s, U_L = 0.001 m/s). CFD simulations are compared with the predictions of the analytic model given by Eqs. (11)–(15).

4 Conclusions

In this paper we have developed a CFD model for describing a bubble column reactor for carrying out a consecutive first-order reaction sequence A → B → C. The bubble column reactor is assumed to operate in the homogeneous bubbly flow regime. The following major conclusions can be drawn from this study:

– For the 0.1 m diameter column (configuration I), 2-D axisymmetric and 3-D transient simulations yield nearly the same results for gas holdup ε_G, centerline liquid velocity $V_L(0)$, conversion of A, χ_A, and selectivity to B, S_B.
– In sharp contrast to above, for the 1 m diameter column (configuration III), there are significant differences in the CFD predictions of ε_G, $V_L(0)$, χ_A, and S_B using 2-D and 3-D simulations; the 2-D strategies tend to exaggerate $V_L(0)$, and underpredict ε_G, χ_A, and S_B. The transient 3-D simulation results appear to be more realistic.
– The CFD simulation results for χ_A and S_B are also compared with a simple analytic model, often employed in practice, in which the gas phase is assumed to be in plug flow and the liquid phase is well mixed. For the smaller diameter columns (configurations I and II) the CFD simulation results for χ_A are in excellent agreement with the analytic model, but for the larger 1 m diameter column the analytic model is somewhat optimistic. There are two reasons for this deviation. Firstly, the gas phase is not in perfect plug flow and secondly, the liquid phase is not perfectly mixed.

The computational results obtained in this paper demonstrate the power of CFD for predicting the performance of bubble column reactors. CFD simulations appear to be particularly powerful in their ability to describe scale effects. However, our studies underline the need for carrying out transient 3-D simulations for sufficiently long times to allow proper determination of quasi-steady-state parameters.

Acknowledgement

The Netherlands Organisation for Scientific Research (NWO) is gratefully acknowledged for providing

financial assistance in the form of a "programmasubsidie" for the development of novel concepts in reactive separation technology.

Received: October 29, 2003 [CET 1968]

Symbols used

a	[$m^2\ m^{-3}$]	interfacial area per unit volume of dispersion
C_D	[–]	drag coefficient, dimensionless
C_G	[–]	gas phase concentration, arbitrary units
C_L	[–]	liquid phase concentration, arbitrary units
C^*_L	[–]	equilibrium liquid phase concentration, arbitrary units
d_b	[m]	diameter of bubble
$Đ_k$	[$m^2\ s^{-1}$]	diffusivity in phase k
D_T	[m]	column diameter
Eö	[–]	Eötvös number, $g\ (\rho_L-\rho_G)d_b^2/\sigma$
F	[s^{-1}]	flux of mass tracer, a.u.
g	[$m\ s^{-2}$]	gravitational acceleration, 9.81 $m\ s^{-2}$
g	[$m\ s^{-2}$]	gravitational vector
h	[m]	height above the distributor at bottom of reactor
H_T	[m]	total height of reactor
He	[–]	Henry coefficient, dimensionless
k_A	[s^{-1}]	first-order reaction rate constant defined in Eq. (9)
k_B	[s^{-1}]	first-order reaction rate constant defined in Eq. (9)
k_L	[m/s]	mass transfer coefficient in liquid phase
M	[N/m^3]	interphase momentum exchange term
NTU	[–]	number of mass transfer units, see Eq. (12), dimensionless
NRU	[–]	number of reaction units, see Eq. (12), dimensionless
p	[Pa]	pressure
r	[m]	radial coordinate
r_a	[s^{-1}]	production/consumption through reaction of component α, a.u.
S	[–]	selectivity, dimensionless
t	[s]	time
u	[m/s]	velocity vector
U	[$m\ s^{-1}$]	superficial fluid velocity
$V_G(r)$	[$m\ s^{-1}$]	radial distribution of gas velocity
$V_L(r)$	[$m\ s^{-1}$]	radial distribution of liquid velocity
$V_L(0)$	[$m\ s^{-1}$]	centerline liquid velocity

Greek symbols

χ	[–]	conversion, dimensionless
ε	[–]	total holdup, dimensionless
$\varepsilon_G(r)$	[–]	radial distribution of gas holdup, dimensionless
μ	[Pa s]	viscosity of fluid phase
ρ	[$kg\ m^{-3}$]	density of phase
σ	[$N\ m^{-1}$]	surface tension of liquid phase

Superscripts

*	equilibrium value

Subscripts

A	referring to component A
B	referring to component B
b	referring to bubbles
eff	effective
G	referring to gas
in	referring to inlet to reactor
L	referring to liquid
out	referring to outlet of reactor
k,l	referring to phase k and l respectively
top	referring to the top of the column
T	tower or column
z	in vertical (axial) direction
a	referring to tracer component α

References

[1] R. Krishna, M. I. Urseanu, J. M. van Baten, J. Ellenberger, *Chem. Eng. Sci.* **1999**, *54*, 4903.
[2] A. Forret, J.-M. Schweitzer, T. Gauthier, R. Krishna, D. Schweich, *Chem. Eng. Sci.* **2003**, *58*, 719.
[3] W. D. Deckwer, *Bubble Column Reactors*, John Wiley, New York, NY, **1992**.
[4] J. W. A. De Swart, R. Krishna, *Chem. Eng. Process.* **2002**, *41*, 35.
[5] S. Degaleesan, S. Roy, S. B. Kumar, M. P. Dudukovic, *Chem. Eng. Sci.* **1996**, *51*, 1967.
[6] S. Degaleesan, M. P. Dudukovic, *AIChE J.* **1998**, *44*, 2369.
[7] R. Krishna, M. I. Urseanu, J. M. van Baten, J. Ellenberger, *Chem. Eng. J.* **2000**, *78*, 43.
[8] M. V. Kantak, R. P. Hesketh, B. G. Kelkar, *Chem. Eng. J. Biochem. Eng. J.* **1995**, *59*, 91.
[9] H. A. Jakobsen, B. H. Sannaes, S. Grevskott, H. F. Svendsen, *Ind. Eng. Chem. Res.* **1997**, *36*, 4050.
[10] J. B. Joshi, *Chem. Eng. Sci.* **2001**, *56*, 5893.
[11] Y. Pan, M. P. Dudukovic, M. Chang, *Chem. Eng. Sci.* **1999**, *54*, 2481.
[12] J. Sanyal, S. Vasquez, S. Roy, M. P. Dudukovic, *Chem. Eng. Sci.* **1999**, *54*, 5071.
[13] A. Sokolichin, G. Eigenberger, *Chem. Eng. Sci.* **1999**, *54*, 2273.
[14] R. Krishna, J. M. van Baten, *Chem. Eng. Res. Des.* **2001**, *79*, 283.
[15] R. Krishna, J. M. van Baten, M. I. Urseanu, *Chem. Eng. Technol.* **2001**, *24*, 451.
[16] R. Krishna, J. M. van Baten, M. I. Urseanu, *Chem. Eng. Sci.* **2000**, *55*, 3275.
[17] R. Krishna, J. M. van Baten, *Chem. Eng. Technol.* **2002**, *25*, 1015.
[18] R. Krishna, J. M. van Baten, *Catal. Today* **2003**, *79*, 67.
[19] J. M. van Baten, R. Krishna, *Chem. Eng. Sci.* **2001**, *56*, 503.
[20] R. Clift, J. R. Grace, M. E. Weber, *Bubbles, Drops and Particles*, Academic Press, San Diego, CA, **1978**.
[21] C. M. Rhie, W. L. Chow, *AIAA J.* **1983**, *21*, 1525.
[22] J. van Doormal, G. D. Raithby, *Numer. Heat Transfer* **1984**, *7*, 147.
[23] U. Jordan, A. Schumpe, *Chem. Eng. Sci.* **2001**, *56*, 6267.
[24] H. M. Letzel, J. C. Schouten, R. Krishna, C. M. van den Bleek, *Chem. Eng. Sci.* **1999**, *54*, 2237.

